



Bergische Universität Wuppertal

Fakultät für Mathematik und Naturwissenschaften

Institute of Mathematical Modelling, Analysis and Computational
Mathematics (IMACM)

Preprint BUW-IMACM 22/10

Lokahith Agasthya, Andreas Bartel, Luca Biferale,
Matthias Ehrhardt and Federico Toschi

**Lagrangian instabilities in thermal convection
with stable temperature profiles**

April 21, 2022

<http://www.imacm.uni-wuppertal.de>

Banner appropriate to article type will appear here in typeset article

1 Lagrangian instabilities in thermal convection with 2 stable temperature profiles

3 Lokahith Agasthya^{1 2 3 †}, Andreas Bartel², Luca Biferale¹, Matthias Ehrhardt²
4 and Federico Toschi⁴

5 ¹Department of Physics, University of Rome “Tor Vergata” and INFN, Via della Ricerca Scientifica 1,
6 00133, Rome RM, Italy

7 ²Angewandte Mathematik und Numerische Analysis, Bergische Universität Wuppertal, Gaußstrasse 20
8 D-42119 Wuppertal, Germany

9 ³Computation-based Science and Technology Research Center, The Cyprus Institute, 20 Kavafi Str.,
10 Nicosia 2121, Cyprus

11 ⁴Department of Applied Physics, Eindhoven University of Technology, The Netherlands

12 (Received xx; revised xx; accepted xx)

13 Non-isothermal particles suspended in a fluid lead to complex interactions – the particles
14 respond to changes in the fluid flow, which in turn is modified by their temperature anomaly.
15 Here, we perform a novel proof-of-concept numerical study based on tracer particles that
16 are thermally coupled to the fluid. We imagine that particles can adjust their internal
17 temperature reacting to some local fluid properties and follow simple, hard-wired active
18 control protocols. We study the case where instabilities are induced by switching the
19 particle temperature from hot to cold depending on whether it is ascending or descending
20 in the flow. A macroscopic transition from a stable to unstable convective flow is achieved,
21 depending on the number of active particles and their excess negative/positive temperature.
22 The stable state is characterized by a flow with low turbulent kinetic energy, strongly stable
23 temperature gradient, and no large-scale features. The convective state is characterized by
24 higher turbulent kinetic energy, self-sustaining large-scale convection, and weakly stable
25 temperature gradients. The particles individually promote the formation of stable temperature
26 gradients, while their aggregated effect induces large-scale convection. When the Lagrangian
27 temperature scale is small, a weakly convective laminar system forms. The Lagrangian
28 approach is also compared to a uniform Eulerian bulk heating with the same mean injection
29 profile and no such transition is observed. Our empirical approach shows that thermal
30 convection can be controlled by pure Lagrangian forcing and opens the way for other data-
31 driven particle-based protocols to enhance or deplete large-scale motion in thermal flows.

32 **Key words:** Flow control, Bénard convection, Turbulent convection

33 **MSC Codes** 76F70.

† Email address for correspondence: lnagasthya@gmail.com

Abstract must not spill onto p.2

34 1. Introduction

35 Thermally driven flows play an important role in both nature and industry. They are
36 notoriously hard to predict and control. In the presence of gravity, temperature fluctuations
37 cause density fluctuations, which in turn drive convective motions through buoyancy in the
38 atmosphere (Markowski 2007; Salesky & Anderson 2018), in oceans (Marshall & Schott
39 1999), and especially in idealized systems such as Rayleigh-Bénard convection (Ahlers *et al.*
40 2009; Lohse & Xia 2010), and horizontal convection (Gayen *et al.* 2014).

41 It is well known that the two-way interactions between particles suspended in a fluid
42 and the fluid phase itself are complex and highly nonlinear. They exhibit behaviour such
43 as preferential concentration due to ejection from vortical regions (Cencini *et al.* 2006;
44 Squires & Eaton 1991) and modification of turbulence (Yang & Shy 2005). The dynamics
45 of particles suspended in turbulence plays an important role in several natural as well as
46 industrial processes, for example in the dispersal of pollutants (Fernando *et al.* 2010), clouds
47 (Falkovich *et al.* 2002; Mazin 1999), planet formation (Bec *et al.* 2014), combustion of jet
48 sprays (Irannejad *et al.* 2015).

49 When suspended particles are thermally coupled to the fluid and are non-isothermal,
50 the particles cause local temperature fluctuations in the fluid, which in turn can further
51 modify a turbulent flow, either purely by thermal action or also in conjunction with the
52 momentum-coupling (Carbone *et al.* 2019) while momentum coupling alone can also alter
53 the heat-transfer dynamics of a thermal flow (Elperin *et al.* 1996). Modification of specific
54 thermal flows due to suspended, thermal particles has also been studied, for example in
55 the Rayleigh-Bénard convection (Park *et al.* 2018), where heavy particles with fixed initial
56 temperatures are introduced into a Rayleigh-Bénard convection system. In this case, the
57 particles are found to enhance vertical heat transfer, an effect that is most pronounced when
58 the particle concentration is greatest due to turbulence (preferential concentration), while
59 attenuating turbulent kinetic energy due to momentum-coupling. Furthermore, the feasibility
60 of achieving control of Rayleigh-Bénard convection solely by applying small temperature
61 or velocity fluctuations has been studied (Tang & Bau 1994). Here, deviations from the
62 stable profiles near the thermal boundaries are detected and compensated, leading to stable
63 Rayleigh-Bénard flows well above the critical Rayleigh number and also the possibility of
64 control of flow patterns is given. Increasing the critical Rayleigh number and delaying the
65 onset of convection can further be improved by applying reinforcement learning techniques
66 to apply the temperature fluctuations near the boundary, as shown by (Beintema *et al.* 2020).

67 External radiation acting solely by heating particles suspended in a flow have shown to
68 modify the global motion and to induce turbulent thermal convection. The work of Zamansky
69 *et al.* (2014, 2016) considered a transparent fluid with suspended inertial particles subject to
70 a constant radiation and at local thermal equilibrium with the fluid. Convection induced in
71 such a system was found to be driven by individual plumes rising out of each particle with
72 turbulent kinetic energy being the largest in the presence of a strong particle preferential
73 concentration where the plumes of individual particles are reinforced by one-another due to
74 their spatial proximity. This eventually led to a sustained turbulent thermal convection, albeit
75 with the temperature of the system constantly increasing due to the permanently applied
76 incident radiation.

77 Internally heated convection (IHC) – induced and sustained by the application of a bulk
78 heating term in a fluid – has also been studied as an idealised theoretical model by Wang
79 *et al.* (2021). They consider a uniformly heated domain with the top and bottom walls kept
80 at the same constant temperature. In this scenario, the bulk attains a stationary temperature
81 depending on the strength of the heating and other parameters such as gravity or the height

82 of the domain, while the fixed temperature boundaries works as a sink of heat, ensuring that
83 the temperature does not increase indefinitely.

84 The study of fluid systems where the heating in the bulk rather than boundary forcing is
85 the dominant mode of thermal forcing has important implications for several natural systems.
86 For example, in the mantle of the earth, the radiogenic heating from the decay of radioactive
87 elements plays a significant role in addition to the heat transfer from the hotter inner core (Lay
88 *et al.* 2008). The atmosphere of Venus which contains a high amount of sulphurous gases
89 absorbs a large part of the incoming solar radiation, making this the dominant mode of heat
90 transfer (Tritton 1975) in contrast to the earth where the majority of the radiation is absorbed
91 by the land surface and in-turn forces the atmosphere. The mantle of Venus is driven in large
92 part by internal heating (Limare *et al.* 2015). Finally, in industrial applications, chiefly in the
93 interior of liquid-metal batteries, convection due to internal heating is of crucial importance
94 (Kim *et al.* 2013).

95 In this study we set up a "theoretical experiment" to study the possibility of controlling the
96 global properties of a thermal flow by applying temperature fluctuations locally along particle
97 trajectories. In our proposed idealisation, the particles are equipped with a hard-wired active
98 protocol capable of releasing or absorbing heat by setting the temperature of each Lagrangian
99 tracer as a function of the local velocity field of the underlying fluid background. Our system
100 is internally heated/cooled by these virtual particles so that the average heating term Φ is
101 statistically zero and hence the average temperature attained by the fluid is unchanged by the
102 forcing. The heat injection by the particles is the only energy source for the system, since
103 the horizontal boundaries are periodic and the top and bottom walls are adiabatic. The aims
104 of the set-up are multifold. First, as a proof of concept, we wish to demonstrate that it is
105 possible to invent hard-wired Lagrangian protocols that can cause global flow transitions.
106 Second, we hope to trigger more studies using phenomenological or data-driven approaches
107 to achieve control of complex systems. Finally, by acting on thermal plumes, we hope one
108 can better understand their role in determining the organisation of the global flow.

109 The remainder of the article is organised in the following manner. In Section 2, we
110 introduce the model equations for the system, the particle temperature protocol and describe
111 the numerical experiments conducted. In Section 3, we present and discuss our main findings
112 from the numerical experiments and finally in Section 4, we present our conclusions as well
113 as possible future directions for further investigation.

114 2. Methods

115 The protocol for particle forcing is as follows: virtual tracer particles are initially randomly
116 placed in a 2D region of length L_x and height L_z with a fluid at rest. The initial temperature
117 of the fluid is set to an unstable configuration with warmer temperatures at the bottom of
118 the domain and colder temperatures at the top of the domain. The particles are idealised to
119 have an infinite heat capacity and a temperature determined by an imposed protocol in which
120 rising particles moving vertically upward are warm with a positive temperature T_+ , while
121 the temperature of falling particles is set to $-T_+$ (see figure 1) so the average temperature
122 of the fluid remains constant. The temperature of the fluid near the particle relaxes to the
123 temperature of the particle at a rate proportional to the difference between the local fluid
124 temperature T and the particle temperature T_p , with a relaxation time $\tau = 1/\alpha$.

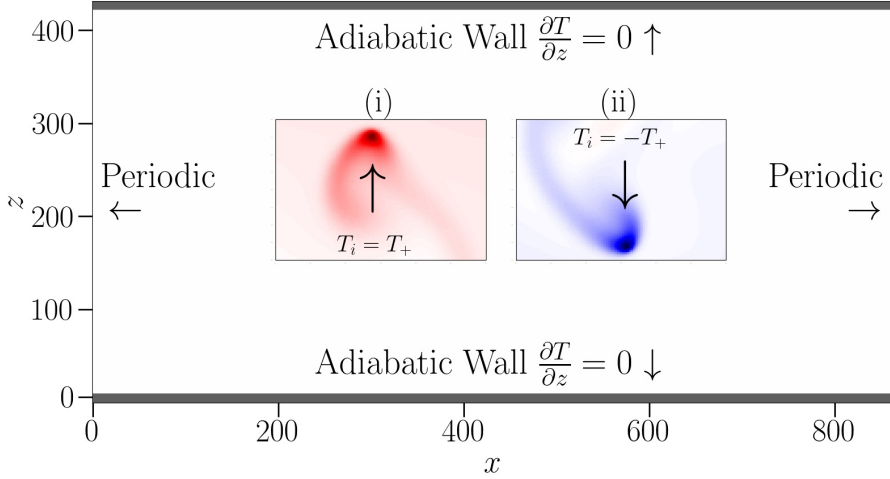


Figure 1: An overview of the methods applied in the study. The domain consists of adiabatic walls at the top and bottom while the lateral boundaries are periodic. In inset (i) and (ii), we show a rising hot particle with temperature T_+ and a falling cold particle with temperature $-T_+$ respectively.

125

2.1. Fluid Equations of Motion

126 The fluid velocity $\mathbf{u} = (u, v)$ and temperature T follow the equations

$$127 \quad \nabla \cdot \mathbf{u} = 0, \quad (2.1)$$

$$128 \quad \partial_t \mathbf{u} + (\mathbf{u} \cdot \nabla) \mathbf{u} = -\nabla p + \nu \nabla^2 \mathbf{u} - \beta T \mathbf{g}, \quad (2.2)$$

$$129 \quad \frac{\partial T}{\partial t} + \mathbf{u} \cdot \nabla T = \kappa \nabla^2 T - \sum_{i=1}^{N_p} \left(\alpha_i(\mathbf{r}, t) [T(\mathbf{r}, t) - T_i(t)] \right). \quad (2.3)$$

130 where (2.1) and (2.2) are the incompressible Navier-Stokes equations for a fluid with unit
 131 density and average temperature $T_0 = 0$ with a buoyancy-force term according to the
 132 Boussinesq approximation, where the density variations are small and enter the equations
 133 only via the gravity-force term. Here p is the fluid pressure, ν is the kinematic viscosity, and
 134 β is the thermal expansion coefficient. Temperature is advected and diffused by Equation
 135 (2.3) where κ the thermal conductivity and the last term on the rhs is a heat source term (i.e.,
 136 a thermal forcing) that depends on the particles (see later).

137 The domain is periodic in the horizontal x -direction while the top and bottom walls at
 138 $z = 0$ and $z = L_z$ are adiabatic with $\mathbf{u} = 0$, that is

$$139 \quad \partial_z T|_{z=0} = \partial_z T|_{z=L_z} = 0, \quad (2.4)$$

$$140 \quad \mathbf{u}(z=0) = \mathbf{u}(z=L_z) = 0. \quad (2.5)$$

141 Note that the only source of energy injected into the system is the heat supplied by the
 142 particles.

2.2. Equations of Particle Motion

143

144 Each particle is assumed to be a point-like tracer. The N_p particles with positions
145 $\{\mathbf{r}_1, \mathbf{r}_2, \dots, \mathbf{r}_{N_p}\}$ and temperatures $\{T_1, T_2, \dots, T_{N_p}\}$ follow the local fluid velocity

$$146 \quad \frac{d\mathbf{r}_i}{dt} = \mathbf{u}(\mathbf{r}_i(t), t). \quad (2.6)$$

147 To mimic an effective particle size, concerning its thermal properties, we imagine that
148 each particle exerts a thermal forcing on the fluid in its immediate vicinity up to a cut-off
149 distance η . The feedback of the particle is defined as a local heat injection term proportional
150 to the difference between the underlying fluid temperature, at the location of the particle, and
151 the instantaneous particle temperature. Furthermore, to have a smooth thermal forcing, we
152 assume that the strength of the coupling α_i (with dimension inverse of time) between the i -th
153 particle and the fluid at time t and position \mathbf{r} has the form of a Gaussian with a peak at the
154 particle location $\mathbf{r}_i(t)$ (see inset (ii) of Fig. 1), given by

$$155 \quad \alpha_i(\mathbf{r}, t) = \begin{cases} \alpha_0 \exp\left(-\frac{|\mathbf{r} - \mathbf{r}_i(t)|^2}{2c^2}\right), & \text{if } |\mathbf{r} - \mathbf{r}_i(t)| \leq \eta, \\ 0, & \text{if } |\mathbf{r} - \mathbf{r}_i(t)| > \eta. \end{cases} \quad (2.7)$$

156 Here, α_0 is the coupling strength at the particle location and c is the size of the virtual particle
157 (referred to as particle size). In fact, c determines the sharpness of the peak of the Gaussian
158 function α_i : the Gaussian peaks more sharply and falls off more quickly for smaller c . On
159 the other hand, η is simply a cut-off length for the thermal forcing by the particle. Thus, the
160 thermal forcing due to the i -th particle Φ_i at location \mathbf{r} is

$$161 \quad \Phi_i(\mathbf{r}, t) = -\alpha_i(\mathbf{r}, t) [T(\mathbf{r}, t) - T_i(t)], \quad (2.8)$$

162 and the total thermal forcing at a given location \mathbf{r} due to all N_p particles reads

$$163 \quad \Phi(\mathbf{r}, t) = -\sum_{i=1}^{N_p} \left(\alpha_i(\mathbf{r}, t) [T(\mathbf{r}, t) - T_i(t)] \right). \quad (2.9)$$

164 To summarise, each particle influences a fixed region surrounding itself and when two
165 particles are within distance 2η , their thermal effects are additive in the overlapping region.

2.3. Particle Temperature Policy

166

167 The temperatures of the particles are determined by a binary policy where the i -th particle
168 has either a positive value T_+ or a negative value $-T_+$ depending on the sign of the vertical
169 velocity of the particle $v_i(t)$:

$$170 \quad T_i = \begin{cases} T_+, & \text{if } v_i > 0, \\ -T_+, & \text{if } v_i < 0. \end{cases} \quad (2.10)$$

171 Since the particle is a tracer, v_i is the same as the vertical velocity of the fluid at the particle
172 location $v(\mathbf{r}_i, t)$. T_+ is a parameter that sets the temperature scale of the system. By heating
173 the upward moving fluid regions and conversely, cooling the downward moving regions, this
174 policy should enhance thermal convection by amplifying any updrafts or downdrafts if they
175 exist. Particles are coupled to each other via their effects on the fluid and because of the flow
176 thermal diffusivity.

177 Our policy leads to a sharp discontinuity in the particle temperature when the particle
178 changes direction. Furthermore, the temperature would rapidly fluctuate between T_+ and $-T_+$
179 at the top and bottom walls where the velocity is very small and the flow is mainly horizontal.
180 To ensure that this doesn't affect our results, we verified that setting $T_i = 0$ for particles within

Parameter	L_x	L_y	ν	κ	α_0	T_+	g	c	β	N_p
Range	864	432	$\frac{1}{1500}$	$\frac{1}{1500}$	[0.0001– 0.005]	$[2.5 \times 10^{-8} -$ 0.05]	8×10^{-6}	$[0.5 -$ $\sqrt{2}]$	1	[48 – 960]

Table 1: List of parameters used in the study along with the range of values in simulation units.

181 one grid length from the top and bottom walls, where the vertical velocity of the particle
182 fluctuates rapidly from small positive values to small negative values, leads to (statistically)
183 the same flows. We have also verified that all results reported below are robust against small
184 change of the above protocol, e.g. by setting a threshold velocity v_0 such that $T_i = 0$ when
185 $|v| < v_0$.

186 2.4. Numerical Experiments

187 The fluid equations (2.1)–(2.3) are solved by the Lattice-Boltzmann method (see Appendix A
188 for details), together with the particle evolution as a tracer given by equation (2.6). The
189 particle evolution is solved by the two-step Adams-Bashforth method. We start from an
190 initially unstable vertical temperature profile of

$$191 \quad T(z) = T_+ \tanh\left(\frac{L_z}{2} - z\right). \quad (2.11)$$

192 The two-way coupled particle-fluid system is evolved until the flow reaches a statistically sta-
193 tionary kinetic energy independent of the initial conditions for the flow velocity, temperature
194 and particles positions. All measurements and analyses are performed at this steady state for
195 different sets of parameters, varying T_+ , N_p , α_0 , and c . The cut-off distance for the particles
196 η is kept constant throughout the study.

197 All results presented in this study are for a 2D fluid domain resolved with 864 grid points
198 in the horizontal direction and 432 grid points in the vertical direction. With the Lattice
199 Boltzmann grid spacing $\Delta x = 1$, we have $L_x = 864$ and $L_z = 432$. The particles have a fixed
200 cut-off distance $\eta = 3$ in computational units, while their size c , is varied. α_0 is varied from
201 10^{-4} to 5×10^{-3} in simulation units. The temperature T_+ is varied over several orders of
202 magnitude. All temperatures in this study are reported in units of $T_s/0.025$ where T_s is the
203 temperature in simulation units. Thus, $T = 0.1$ corresponds to a temperature of $T_s = 0.0025$
204 in simulation units. This convention is chosen solely to make it easier to compare the scales
205 of the various T_+ and make the manuscript more readable. The values of the parameters are
206 summarised in table 1.

207 In order to have dimensionless quantities, we define a *typical velocity* u_0 , given by

$$208 \quad u_0 = \sqrt{cg\beta \frac{\alpha_0}{\alpha_0 + \frac{\kappa}{2c^2}} T_+}, \quad (2.12)$$

209 where c is the size of the particle as defined in equation (2.7). The form (2.12) was suggested
210 by studying the evolution of single particles experiments at varying α_0 and c , where the rms
211 value of the vertical particle velocity was found to scale as in (2.12). In particular, we find
212 that the particle velocity statistics remain independent of the domain height L_z , justifying
213 the choice of c as the length scale of the system. The fluid near the particle relaxes to the

214 temperature of the particle, and this relatively hotter/cooler local plume rises/falls. The tracer
 215 particle in turn responds to the fluid and accelerates at a rate that depends on the temperature
 216 anomaly, gravity g and β . This is similar to other thermal flows such as Rayleigh-Bénard
 217 convection. The local heating is high when c is large because a wider region around each
 218 particle is thermally forced. The quantity

$$219 \quad T_a = \frac{\alpha_0}{\alpha_0 + \frac{\kappa}{2c^2}} T_+ \quad (2.13)$$

220 is interpreted as an *effective temperature* reached in the vicinity of each particle. The empirical
 221 prefactor $\alpha_0/(\alpha_0 + \frac{\kappa}{2c^2})$ by which T_+ is multiplied is a constant that gives the rate of relaxation
 222 of the fluid temperature to the particle temperature compared with the rate at which heat is
 223 diffused away from the particle by conduction, which is proportional to κ/c^2 . When $\alpha_0 \rightarrow 0$,
 224 then $T_a \rightarrow 0$, because the fluid is no longer coupled to the particle and there is no energy
 225 input to the system. When $\alpha_0 \gg \kappa/c^2$, then $T_a \rightarrow T_+$, meaning the fluid attains the local
 226 particle temperature. For large κ , the heat is rapidly conducted away from the tracer so that
 227 effective temperature is lower, where again $T_a \rightarrow 0$ when $\kappa \rightarrow \infty$ while the case of small κ
 228 is similar to that of large α_0 . In our study, α_0 and κ/c^2 are of comparable magnitude.

229 Furthermore, we define the normalized *turbulent kinetic energy* $E_k(t)$ of the system as

$$230 \quad E_k(t) = \frac{1}{2} \frac{\langle |\mathbf{u}(t)|^2 \rangle_V}{u_0^2 N_p}, \quad (2.14)$$

231 where $\langle \cdot \rangle_V$ represents the average over the entire domain at a given time. We also define with
 232 an overline \overline{E}_k as the average normalized turbulent kinetic energy (TKE), i.e.

$$233 \quad \overline{E}_k = \langle E_k(t) \rangle_t, \quad (2.15)$$

234 where $\langle \cdot \rangle_t$ denotes the time average after the flow reaches a statistically stationary regime. If
 235 the particles are sparse and their motion is independent of each other, the kinetic energy of the
 236 system would simply be a sum of the motion of the individual particles and we would expect
 237 E_k to remain constant. However, if the motions of the particles are not merely additive, but
 238 cause a large-scale flow in the system, we would expect E_k to increase as a function of N_p .

239 3. Results

240 3.1. Stable and Convective Configurations

241 First, we vary the number of virtual particles N_p . Figure 2 shows four cases, where we
 242 visualize snapshots of the temperature and velocity fields. Thereby the rising particle
 243 temperature T_+ , particle-fluid coupling strength α_0 and particle size c are fixed. The figure
 244 indicates that there are two distinct stationary typical configurations. The first, which we
 245 term *stable*, is shown in the top panels (a) and (b) of figure 2. In this state, kinetic energy
 246 is low and large scale circulation is absent. Particles are either nearly still and close to
 247 the top and bottom walls or they execute a slow vertical motion independently one from
 248 the others, propelled by their higher or lower temperature compared to the bulk. When the
 249 particle concentration reaches beyond a certain threshold, the individual thermal effect of the
 250 particles aggregates and triggers a transition to a second state shown in the bottom panels
 251 (c) and (d) of figure 2. This convective state enjoys a large scale circulation, the presence
 252 of rising and falling plumes with the particles trajectories synchronized with the large-scale
 253 recirculation regions. In figure 2, this transition occurs for $N_p \sim 150$.

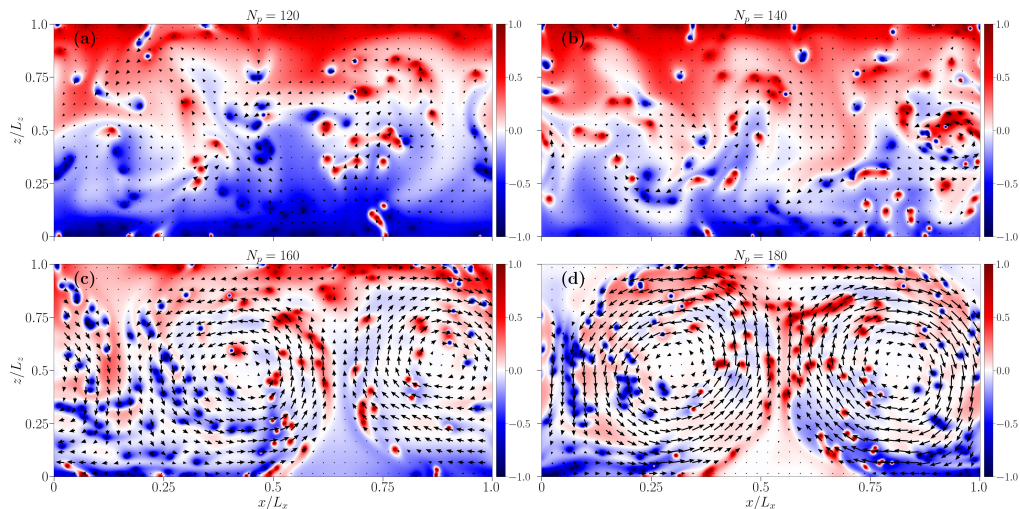


Figure 2: Snapshots of the temperature field $T(\mathbf{r}, t)/T_+$ at a given instant of time for $T_+ = 0.1$, $\alpha_0 = 0.005$, $c = 1$ and at changing $N_p = 120, 140, 160, 180$ in panels (a), (b), (c) and (d), respectively. The colour palette varies from red to blue where red indicates $T = T_+$ and blue indicates $T = -T_+$. The black arrows show the velocity field with the length of the arrow representing the relative magnitude of the velocity with identical scaling for all four panels. The top panels show a stable configuration while the bottom panels show a convective configuration.

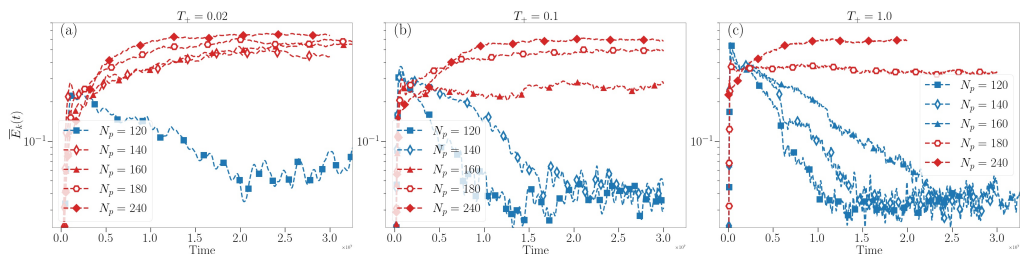


Figure 3: Time evolution of $E_k(t)$ for flows with (a) $T_+ = 0.02$, (b) $T_+ = 0.1$ and (c) $T_+ = 1.0$ with $\alpha_0 = 0.005$ and $c = 1$ kept fixed. Stable configurations are plotted in blue while convective configurations are plotted in red. The time is in simulation time units.

254 In figure 3 we show the time evolution of the TKE for parameters before and after the
 255 transitions. Panels (a), (b) and (c) corresponds to $T_+ = 0.02$, $T_+ = 0.1$ and $T_+ = 1.0$,
 256 respectively, with α_0 and c remaining fixed. The blue curves represent stable configurations
 257 while the red curves represent convective configurations. The kinetic energy first increases
 258 due to the unstable temperature gradient imposed on the initial condition. At later times,
 259 the thermal forcing by the tracers is dominant and the flow attains a statistically stationary kinetic
 260 energy where $E_k(t)$ either shows a large value (red curves), corresponding to a convective
 261 flow shown qualitatively in figure 2 or a low value (blue curves) corresponding to a quasi
 262 stable flow.

263 Two further points are note-worthy about the transition from figure 3. Firstly, the transition
 264 is abrupt: it is enough to add very few particles to have a jump $\gtrsim 5$ in the normalised
 265 kinetic energy. It should be noted that the expression of $E_k(t)$ is normalized by N_p in the
 266 denominator, so the absolute increase in kinetic energy is even greater. Secondly, the critical

267 N_p depends slightly on T_+ , where for larger T_+ , the transition occurs at a slightly larger N_p .
 268 We see that in panel (a) with $T_+ = 0.02$, the transition lies between $N_p = 120$ and $N_p = 140$
 269 while in panel (c) with $T_+ = 1.0$, the transition lies between $N_p = 160$ and $N_p = 180$, with
 270 the case of $T_+ = 0.1$ in panel (b) showing an intermediate behavior. This weak dependence
 271 on T_+ which will be further commented upon later. It has been verified that the transitions
 272 are robust by replacing the initial unstable profile with an initial temperature field of $T = 0$
 273 everywhere with particles being either hot or cold with probability 0.5 each.

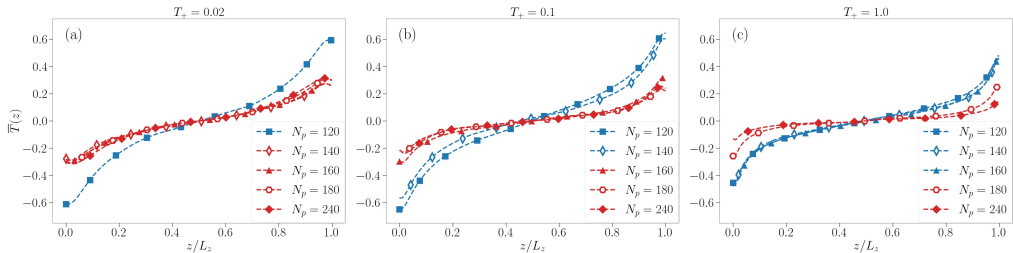


Figure 4: Time-averaged vertical temperature profile divided by T_+ plotted against the vertical height for various N_p close to the transition N_p for $T_+ = 0.02$ (a), $T_+ = 0.1$ (b) and $T_+ = 1.0$ (c). Stable configurations are plotted in blue while convective configurations are shown in red.

274 In figure 4, we show a comparison of the normalised time-averaged vertical temperature
 275 profiles $\bar{T}(z)$ for the same set of flows given by

$$276 \quad \bar{T}(z) = \frac{\langle T(\mathbf{r}, t) \rangle_{x,t}}{T_+}, \quad (3.1)$$

277 where $\langle \cdot \rangle_{x,t}$ represents the time-average at a given height z . Notice that the temperature
 278 gradients for the stable flows (blue) show a strongly stable profile ($\partial_z T > 0$) while the
 279 convective flows still show an overall stable temperature profile but with weaker gradients
 280 so that the temperature difference between the top and the bottom adiabatic walls are much
 281 smaller. In the presence of a large-scale circulation, the temperature field is more effectively
 282 transported and mixed throughout the domain. We also see that with increase in T_+ , the stable
 283 configurations show a flatter temperature profile for the corresponding N_p of lower T_+ flows,
 284 i.e., for example, the red curves in panel (c) are much flatter than those in panel (a).

285 The dual-nature of the effect of the virtual particles is observed here – the particles tend
 286 to make the flow more stable by carrying heat away from the lower half of the domain
 287 while carrying heat towards the upper half of the domain. Thus, the larger T_+ is, the more
 288 stable the system becomes. However, when a certain threshold of particles is reached, the
 289 situation changes – the virtual particles together create a persistent large-scale flow and now
 290 the convection is strong enough to overcome the stable temperature gradient.

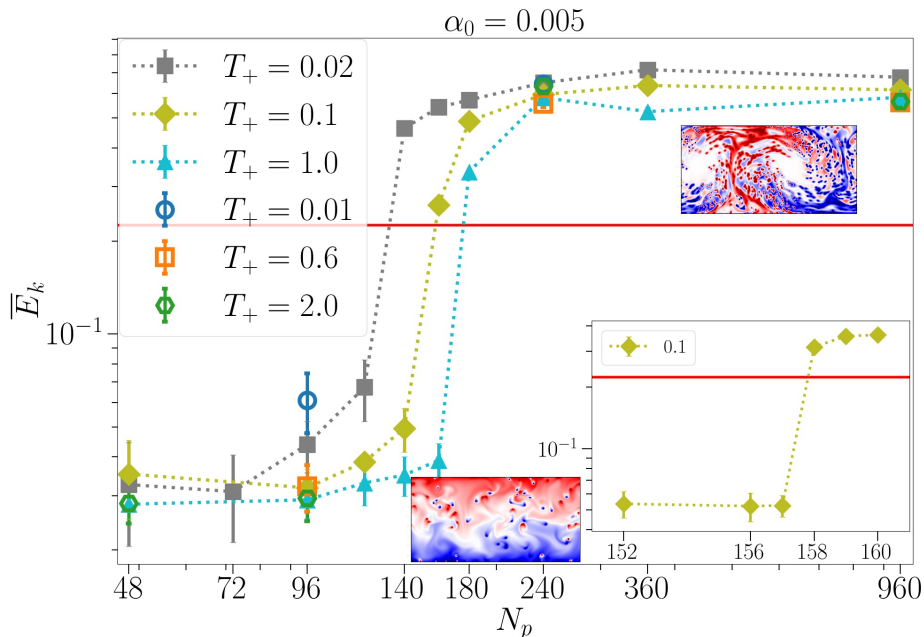


Figure 5: Time averaged normalized TKE \overline{E}_k as a function of N_p for various T_+ (shown in legend) for $\alpha_0 = 0.005$ and $c = 1$. The inset (in the lower right corner) shows the behavior of a flow with $T_+ = 0.1$ very close to the transition N_p . Also shown are instantaneous snapshots of the temperature field for a stable configuration (bottom) and a convective configuration (top right). The error bars indicate the standard deviation of the temporal fluctuations of $E_k(t)$ around the average kinetic energy in the stationary regime.

291 In figure 5, we take a closer look at the transition by plotting the average normalised TKE
 292 of the flows as defined in equation (2.15) against N_p , for the same α_0 as above, for various
 293 T_+ . The sharp increase of TKE at a transition N_p is once again clearly visible. We empirically
 294 define a value of $E_k^0 = 0.225$ indicated by the horizontal red line as the transition point where
 295 for stable end states, $\overline{E}_k < E_k^0$ and vice-versa for the convective end state. The sharpness of
 296 the transition is examined more closely in the inset of the figure for a given T_+ . It is seen
 297 that the transition occurs for an increase of just one single particle. The dependence of the
 298 transition on T_+ is weak, for T_+ varying over 2 orders of magnitude the transition occurs at
 299 nearly the same N_p .

300 3.2. Large-scale Circulation and Heat Transfer

301 While the existence of the large-scale circulation is apparent from the visualisations of the
 302 temperature and velocity fields, it is possible to infer its presence quantitatively from the fluid
 303 energy spectrum. In particular, we consider the spectrum in the horizontal direction taken at
 304 the mid-plane $z_0 = L_z/2$, given by

$$305 E_{\mathbf{u}}(k_x) = \frac{1}{2} \left\langle |\hat{\mathbf{u}}(k_x, z_0, t)|^2 \right\rangle_t, \quad (3.2)$$

306 and $\hat{\mathbf{u}}(k_x, z_0, t)$ are the Fourier coefficients of the field \mathbf{u} and $\langle \cdot \rangle_t$ denotes the time averaging.
 307 We denote by E_1 the energy contained in the first Fourier mode with wavenumber $k_x =$
 308 $2\pi/L_x$, E_2 is used for energy of the second mode ($k_x = 4\pi/L_x$), and so on. Moreover, we

309 define E_{tot} as the sum of the energy contained in all the Fourier modes,

$$310 \quad E_{\text{tot}} = \sum_{i=1}^{N_k} E_i, \quad (3.3)$$

311 where N_k is the Fourier mode corresponding to the smallest resolved length-scale. The
 312 strength of the large-scale circulation with a rising plume and a falling plume can be measured
 313 by the value E_1/E_{tot} (Xi *et al.* 2016), which measures the fraction of energy contained in
 314 the first mode, that is the smallest wave number. This corresponds to a cosine mode for
 315 the velocity field in the bulk, which is a close approximation when there exist two counter-
 316 rotating vortices. When such a large-scale flow is present, we would have $E_1/E_{\text{tot}} \gg 0$,
 317 while if the flow lacks large-scale convection, we would have a flatter energy spectrum with
 318 $E_{\text{tot}} \gg E_1$ and $E_1 \sim E_2$.

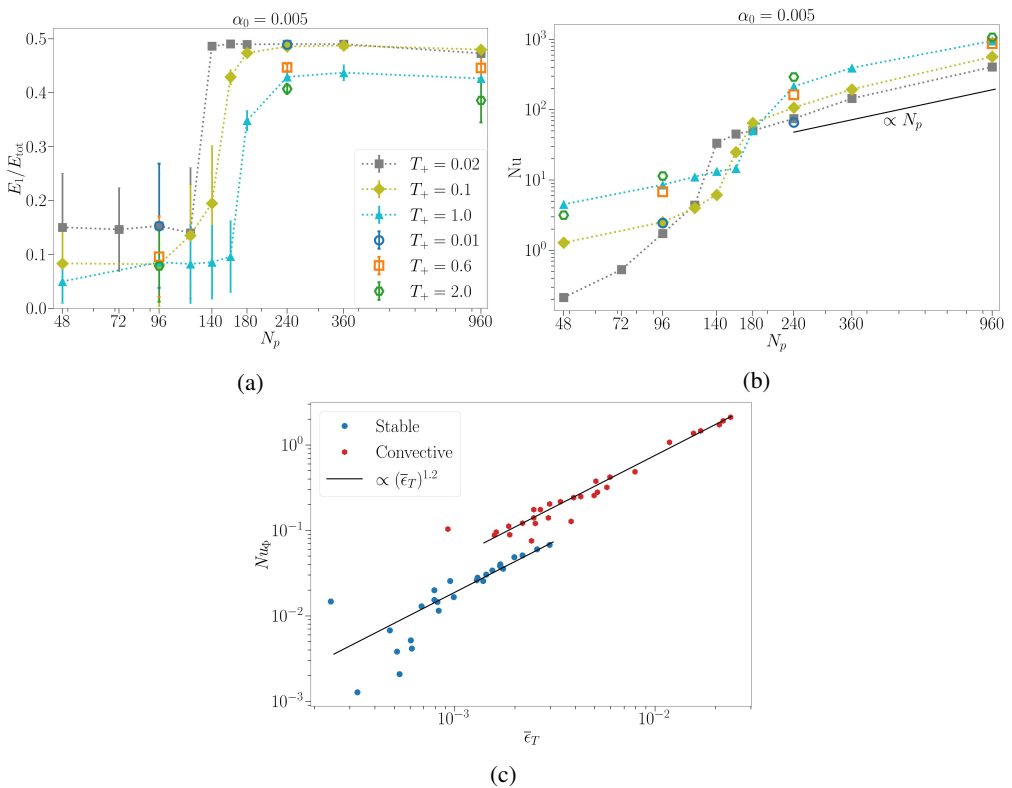


Figure 6: (a) E_1/E_{tot} for varying N_p for various values of T_+ . Error bars show the temporal fluctuations of E_1/E_{tot} (b) Nu for varying N_p for various values of T_+ . The black solid line shows a linear scaling with N_p . (c) Plot of the average normalised Nusselt number Nu_{top} against the average normalised thermal energy injection $\bar{\epsilon}_T$ for flows with varying parameters. Stable flows are marked with blue filled circles, convective with red filled hexagons and the two black lines scale as $(\bar{\epsilon}_T)^{1.2}$

319 In figure 6(a), we plot the strength of the large-scale circulation E_1/E_{tot} for varying N_p .
 320 We see clearly here that corresponding to a jump in the magnitude of the TKE seen in
 321 figure 5, there is also a similar large increase in the ratio of kinetic energy contained in the
 322 largest-scale. Given that \bar{E}_k takes into account the typical velocity of a single particle as

323 well as the number of particles, the excess kinetic energy clearly comes from the large-scale
 324 circulation that arises after the transition, a cumulative particle effect.

325 Figure 6(b) shows the dimensionless Nusselt number, Nu , defined as

$$326 \quad Nu = \frac{\left\langle vT - \kappa \frac{\partial T}{\partial z} \right\rangle_{V,t}}{\frac{\kappa \overline{\Delta T}}{L_z}}, \quad (3.4)$$

327 where $\langle \cdot \rangle_{V,t}$ represents average over the entire domain and time, v is the vertical fluid velocity
 328 and $\overline{\Delta T}$ is the time-averaged temperature difference between the top and bottom walls given
 329 by

$$330 \quad \overline{\Delta T} = \langle T(x, L_z) \rangle_{x,t} - \langle T(x, 0) \rangle_{x,t}. \quad (3.5)$$

331 Here, the Nusselt number is defined in analogy with Rayleigh-Bénard convection: it is the
 332 ratio of heat transfer due to convection and the heat transfer by conduction with the difference
 333 that the temperature jump is taken in the opposite sense because of the presence of a stable
 334 mean profile. Due to the adiabatic boundary conditions imposed at the top and bottom walls
 335 ($\partial_z T = 0$) along with the no-slip boundary condition for the velocity ($\mathbf{u} = 0$), the value of the
 336 Nusselt number is 0 at the top and bottom walls. Thus, the boundary walls do not contribute
 337 to the heat transfer. The Nusselt number naturally increases proportionally with the number
 338 of particles.

339 We see in figure 6(b) that the value of Nu increases gradually with increase in N_p , followed
 340 by a large increase around the transition N_p and then settling to a roughly linear increase with
 341 N_p in the convective regime. The reason for the large increase of Nu at the transition is two-
 342 fold. Firstly, the increase in TKE overall leads to an increase in the convective heat transfer
 343 which further increases vT . Secondly, with more effective mixing of the temperature and a
 344 weakly stable temperature gradient, $\overline{\Delta T}$ in the denominator also has a smaller magnitude.

345 Another way to quantify the heat transfer is to divide it by the typical forcing Φ multiplied
 346 by the length-scale of the system. This is similar to the normalisation procedure of (Wang
 347 *et al.* 2021) applied to internally heated convection (with volume forcing). The effective
 348 temperature T_a defined in equation (2.13) was introduced as a typical value of the temperature
 349 attained by the fluid in the vicinity of the particle with an associated length-scale c for each
 350 particle. In a similar vein, $\alpha_0(T_+ - T_a)$ can be considered the typical thermal forcing acting
 351 on the fluid. We use two dimensionless response parameters of the system. First, we define
 352 the normalised Nusselt number Nu_Φ given by

$$353 \quad Nu_\Phi = \frac{\left\langle vT - \kappa \frac{\partial T}{\partial z} \right\rangle_{V,t}}{c \alpha_0 (T_+ - T_a)}. \quad (3.6)$$

354 Nu_Φ measures the heat transfer by convection relative to the input typical thermal forcing
 355 multiplied by the length scale of the system.

356 In the stationary regime, the thermal dissipation rate ϵ_T is given by $\langle \Phi T \rangle_{V,t}$ (see
 357 Appendix C) and is normalised as

$$358 \quad \bar{\epsilon}_T = \frac{\langle \Phi T \rangle_{V,t}}{\alpha_0 (T_+ - T_a) T_+}. \quad (3.7)$$

359 The normalisation factor is once again the typical forcing multiplied by the temperature scale.

360 In figure 6(c) we plot the normalised Nusselt number Nu_Φ against the normalised thermal
 361 dissipation $\bar{\epsilon}_T$, quantifying the measured convective response of the fluid to the measured
 362 input thermal forcing for varying T_+ , c , α_0 and N_p . It is seen that there exists a global scaling
 363 of these two quantities for both the flow regimes, stable and convective with a rough scaling

364 of $\text{Nu}_\Phi \propto (\bar{\epsilon}_T)^{1.2}$. However, the higher magnitude of the normalised Nusselt number in the
 365 convective case differentiates it from the stable flows.

366 The above findings are consistent with a situation that can be briefly described as such
 367 – individual particles thermally coupled to the fluid have a small zone of influence and
 368 release or absorb heat in their immediate vicinity. Thus, each particle contributes to the
 369 thermal injection into the domain as well as the vertical heat transfer across the domain.
 370 The heat injection as well as vertical heat transfer increase with the increase in number of
 371 particles. In the stable regime, the main effect of the particles is to maintain the strongly
 372 stable temperature gradient. At the transition to the convective regime, the development of
 373 the large-scale convective flow patterns and more turbulent flow leads to a large increase in
 374 the heat transfer relative even to the thermal energy injection, while also seeing a weaker
 375 stable vertical temperature gradient across the domain.

376 3.3. Comparison with Eulerian imposed thermal forcing

377 We consider a thermal fluid system with a thermal forcing $\phi(z)$ uniformly applied at all
 378 times. The forcing is a close approximation of the measured forcing Φ in the Lagrangian
 379 system with the particles in the domain as shown in figure 7. Defining $Q(z)$, the numerator
 380 of the Nusselt number, as the average net heat transfer in the positive z direction at height z
 381 given by

$$382 \quad Q(z) = \left\langle v(\mathbf{r}, t)T(\mathbf{r}, t) - \kappa \partial_z T|_{(\mathbf{r}, t)} \right\rangle_{x,t}, \quad (3.8)$$

383 where $\langle \cdot \rangle_{x,t}$ indicates the time and spatial averages at a given height z , notice that averaging
 384 equation (2.3) over time gives

$$385 \quad \langle \Phi(z) \rangle_{x,t} = \partial_z Q(z). \quad (3.9)$$

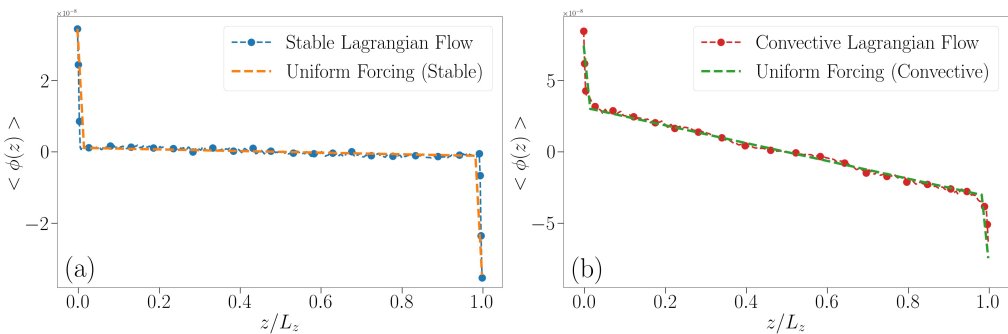


Figure 7: The measured value of the average vertical profile of thermal forcing $\Phi = -\alpha(T - T_p)$ for (a) a stable flow and for (b) a convective flow (b) compared to the imposed vertical profile of the thermal forcing.

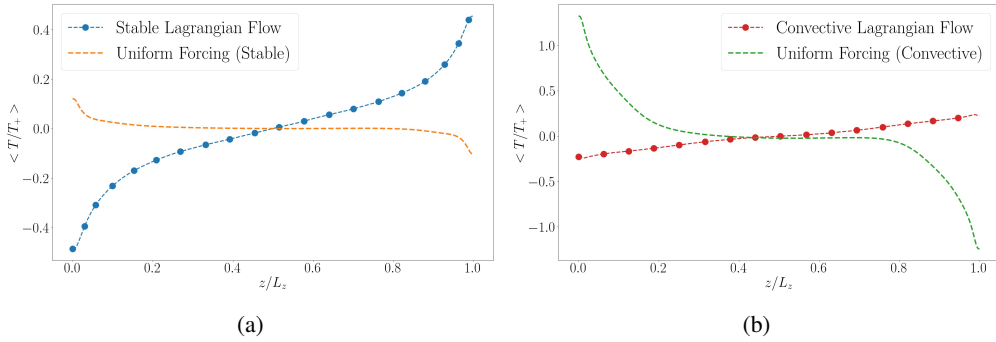


Figure 8: (a) The normalised temperature profile for a stable Lagrangian flow (blue) compared with the measured temperature profile of a flow with an imposed profile of thermal forcing. (b) The normalised temperature profile for a convective Lagrangian flow (red) compared with the measured temperature profile of a flow with an imposed profile of thermal forcing

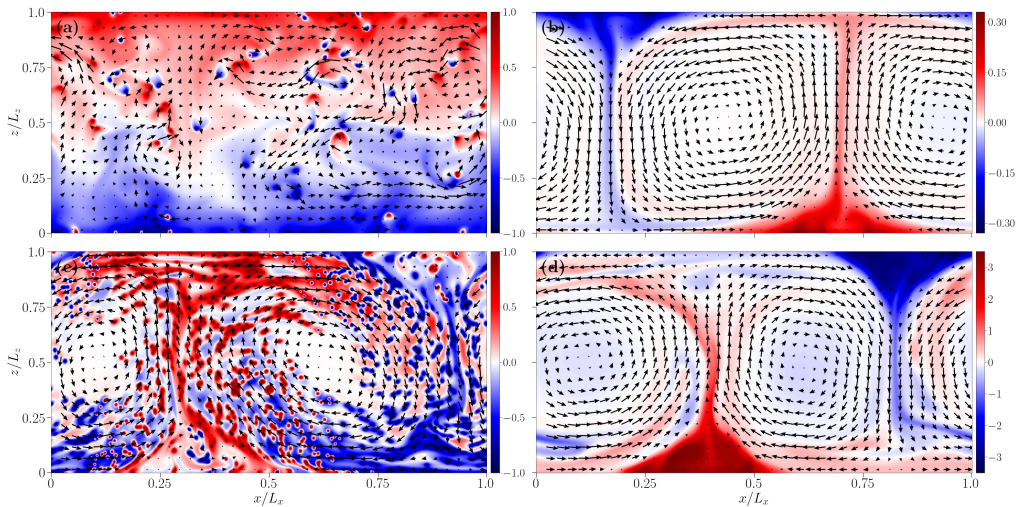


Figure 9: Snapshots of the temperature fields: (a) a stable Lagrangian flow (upper left), (c) a convective Lagrangian flow (lower left), and the two uniformly forced flows to mimic the stable (b) and convective flows (d) in right column. The temperature fields T are divided by the respective T_+ . The black arrows show the velocity field. The length of the arrows indicate the magnitude of the velocity field within each panel – the arrow lengths are scaled differently for different flows to allow for the clearest viewing of the flow structure.

386 The comparison is made for one stable and one convective flow. Given identical vertical
 387 profiles of thermal forcing (see figure 7), one would expect that the resulting temperature
 388 profile and hence the nature of the flows would remain identical. However, as shown
 389 in figure 8, the temperature profiles show a dramatic difference, with the Eulerian flows
 390 showing an unstable temperature profile similar to the Rayleigh-Bénard Convection. Further,
 391 as shown in figure 9, even when the thermal forcing matches the measured value from a stable
 392 configuration, the Eulerian flow with uniform thermal forcing shows a convective behavior
 393 with clear, well-defined hot and cold plumes and an unstable temperature gradient. Even in
 394 the convective case, the corresponding Eulerian flow is convective. Thus, the presence of the
 395 stable temperature gradients and the two typical configurations outlined previously is not a

396 result of the net thermal forcing applied on the system but of the particular Lagrangian nature
 397 of the thermal tracers and the two-way coupling with the fluid.

398 3.4. Anomalous Behavior for Small T_+

399 We have already noted in previous sections that there is weak dependence of the transition
 400 of the system on the value of T_+ . In particular, it was observed that for larger T_+ , the
 401 transition occurs at a larger N_p and the stable configurations for larger T_+ have relatively
 402 flatter temperature gradients. One would conclude then that for any given N_p , there exists a
 403 T_+ small enough such that the system is convective. However, at very small T_+ , the system
 404 attains a third columnar state where the temperature profile is still stable ($\partial_z T > 0$) and the
 405 system has a weak convective flow (see snapshot in figure 10 (b)).

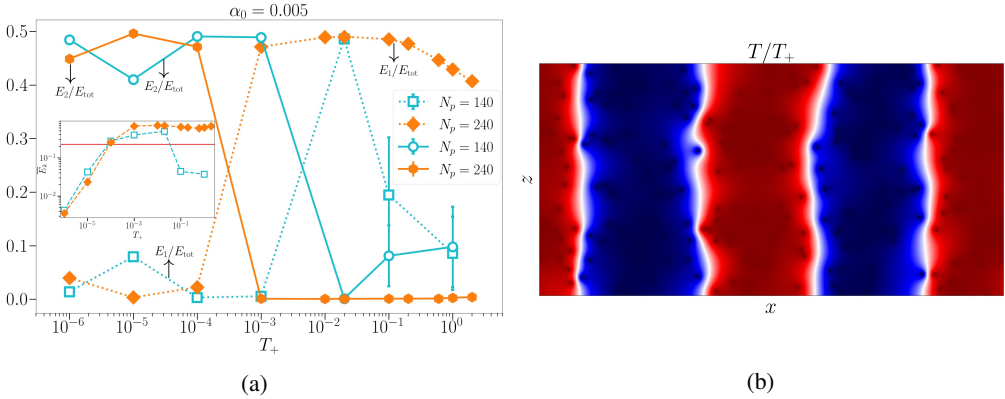


Figure 10: (a) The ratio of kinetic energy contained in the first Fourier mode E_1/E_{tot} (dashed lines) and E_2/E_{tot} (solid lines) to the total energy contained in all modes for $N_p = 140$ and $N_p = 240$ plotted against T_+ . Inset shows the averaged normalised TKE \bar{E}_k for the same parameters and the horizontal line represents $\bar{E}_k = E_k^0$. (b) A snapshot of the temperature field for a columnar flow with $N_p = 240$ and $T_+ = 10^{-5}$. The colour palette varies from red to blue where red indicates $T = T_+$ and blue indicates $T = -T_+$.

406 In figure 10 (a), we plot the fraction of energy contained in the first Fourier mode (E_1/E_{tot})
 407 as well as the second Fourier mode (E_2/E_{tot}) to understand the large-scale behavior of
 408 the flow. We can see clearly that for smaller T_+ , the second mode dominates the kinetic
 409 energy while the energy contained in the first mode approaches 0. This is the case until
 410 a transition T_+ , where now the flow turns convective from columnar, with a dominance of
 411 E_1 . At larger T_+ for $N_p = 240$ (orange, filled symbols), we see that while E_2/E_{tot} remains
 412 small, the value of E_1/E_{tot} shows a decreasing trend. This is because as T_+ is increased, the
 413 flow becomes more turbulent and small-scale velocity features begin to appear, increasing
 414 the energy contained at higher modes. For $N_p = 140$ (cyan, empty symbols), the flow is
 415 columnar for $T_+ \lesssim 10^{-3}$ and transitions to convective at $T_+ \sim 0.02$, as evidenced by the
 416 values of E_1/E_{tot} and E_2/E_{tot} . However, on increasing T_+ further, the flow again moves to
 417 a stable configuration, as evidenced by the fact that $E_1 \sim E_2$ which indicates the lack of
 418 any large-scale velocity flow. This transition is due to the effect already observed, that for
 419 increasing T_+ , the N_p of transition from stable to convective is greater.

420 The inset of figure 10(a) shows the normalised TKE plotted for the two given N_p and
 421 varying T_+ . Notice that at small T_+ , when the flow is columnar, it is characterised by a smaller
 422 normalised TKE and kinetic energy smoothly approaches 0 as $T_+ \rightarrow 0$.

423 **4. Conclusions and Discussion**

424 We have performed numerical simulations of an idealized non-isothermal 2D fluid system
425 under the Boussinesq approximation with suspended tracer particles. The particles act as
426 heat sources or sinks depending on their vertical velocity. The particles are coupled to the
427 fluid only thermally, the fluid is forced only by the action of the particles. Individually, each
428 particle aids in the transport of heat away from the bottom of the domain towards the top of
429 the domain, thus working to create a thermally more stable system. However, under certain
430 conditions, the cumulative effect of the particles overpowers the tendency towards stability
431 and the result is a system with a large-scale convective flow pattern with increased turbulent
432 kinetic energy, larger heat transfer across the domain, maximum energy in the largest Fourier
433 modes and a (weakly) stable vertical temperature gradient. The main parameters of the system
434 are the temperature of the hot, rising particles T_+ , the number of particles N_p , the strength
435 of the thermal coupling between the fluid phase and the particles α_0 and the size of the
436 particle c . Increasing N_p , c and α_0 makes the flow increasingly convective while increasing
437 T_+ weakly contributes to making the flow more stable.

438 This Lagrangian protocol is compared with a system with a uniform thermal forcing
439 identical to the measured Lagrangian forcing and it is found that the temperature profiles of
440 the Eulerian system is unstable rather than stable and a convective flow always develops.

441 Extension to 3D set-ups and to cases with larger domain and/or a larger number of
442 particles to study whether the intensity of turbulence can be increased indefinitely would
443 also be interesting.

444

445 Independently of the possibility to realize a protocol like the one we studied here in a
446 realistic experimental set-up, our study is meant to gain a new insight about the impact
447 of Lagrangian control on turbulent convection. A real-world example would be a cloud
448 of droplets moving along with an updraft – the droplet remains uniformly hotter than the
449 surroundings due to condensation of water onto its surface and similarly, falling cloud droplets
450 constantly lose water to the atmosphere thus remaining cooler while moving downward.

451 Our study also opens several further interesting avenues for investigation including -but
452 not limited to- the formulation of similar protocols where the properties of the suspended
453 particles is optimized by a data-driven approach to attain complex controls and modulation
454 of fluid flows.

455 **Funding**

456 This project has received funding from the European Union's Horizon 2020 research and
457 innovation programme under the Marie Skłodowska-Curie grant agreement No 765048.
458 This work was supported by the European Research Council (ERC) under the European
459 Union's Horizon 2020 research and innovation programme (Grant Agreement No. 882340).

460

461 **Declaration of interests** The authors report no conflict of interest

462 **Data Availability Statement**

463 Data available on request from the authors – The data that support the findings of this study
464 are available from the corresponding author upon reasonable request.

465 Appendix A. Numerical Methods

466 A.1. Lattice Boltzmann Method

467 The fluid equations are solved by the Lattice Boltzmann method with two sets of populations
468 using a standard D2Q9 grid.

$$469 \quad f_i(\mathbf{r} + \mathbf{c}_i \Delta t, t + \Delta t) = f_i(\mathbf{r}, t) - \frac{f_i - f_i^{\text{eq}}}{\tau_f} \Delta t + S_i \Delta t, \quad (\text{A } 1)$$

$$470 \quad g_i(\mathbf{r} + \mathbf{c}_i \Delta t, t + \Delta t) = g_i(\mathbf{r}, t) - \frac{g_i - g_i^{\text{eq}}}{\tau_g} \Delta t + q_i \Delta t. \quad (\text{A } 2)$$

472 The evolution of the two sets of populations f and g , representing the fluid and the thermal
473 phase respectively, follow the Lattice Boltzmann equations with a Bhatnagar–Gross–Krook
474 (BGK) collision operator. The vectors \mathbf{c}_i for $i = 1, \dots, 9$ are the discrete particle velocities, Δt
475 is the lattice time-step, so that $\mathbf{c}_i \Delta t$ go from each lattice point to the 8 nearest neighbouring
476 lattice points in the uniform 2D grid and $\mathbf{c}_0 = 0$. S_i and q_i represent the momentum
477 forcing (buoyancy) and the thermal forcing respectively. The time-step and the grid spacing
478 respectively $\Delta t = \Delta r = 1$, as is the standard practice. f^{eq} and g^{eq} are the equilibrium
479 population distributions as defined in He *et al.* (1998) given by

$$480 \quad f^{\text{eq}} = w_i \rho \left(1 + \frac{\mathbf{u} \cdot \mathbf{c}_i}{c_s^2} + \frac{(\mathbf{u} \cdot \mathbf{c}_i)^2}{2c_s^4} - \frac{\mathbf{u} \cdot \mathbf{u}}{2c_s^2} \right), \quad (\text{A } 3)$$

$$481 \quad g^{\text{eq}} = w_i T \left(1 + \frac{\mathbf{u} \cdot \mathbf{c}_i}{c_s^2} + \frac{(\mathbf{u} \cdot \mathbf{c}_i)^2}{2c_s^4} - \frac{\mathbf{u} \cdot \mathbf{u}}{2c_s^2} \right), \quad (\text{A } 4)$$

483 where w_i are the weights for each population set by the grid used, D2Q9 in this study. c_s is
484 the lattice speed of sound set by the choice of \mathbf{c}_i .

485 τ_f and τ_g are respectively the fluid and the thermal relaxation times which set the values
486 for kinematic viscosity ν and thermal conductivity κ as

$$487 \quad \nu = c_s^2 (\tau_f - 0.5), \quad (\text{A } 5)$$

$$488 \quad \kappa = c_s^2 (\tau_g - 0.5). \quad (\text{A } 6)$$

490 To account for the buoyancy force term, the Guo-forcing scheme (Guo *et al.* 2002) is employed
491 with

$$492 \quad S_i = \left(1 - \frac{\Delta t}{2\tau_f} \right) w_i \left(\frac{\mathbf{c}_i - \mathbf{u}}{c_s^2} + \frac{(\mathbf{c}_i \cdot \mathbf{u}) \mathbf{c}_i}{c_s^4} \right) \cdot \mathbf{F}, \quad (\text{A } 7)$$

493 where \mathbf{F} is the physical force vector.

494 The fluid hydrodynamic quantities at each point in space and time are obtained from the
495 various moments of the populations as

$$496 \quad \rho = \sum_i f_i, \quad (\text{A } 8)$$

$$497 \quad \mathbf{u} = \frac{1}{\rho} \sum_i f_i \mathbf{c}_i + \frac{\mathbf{F}}{2\rho}. \quad (\text{A } 9)$$

499 The ease of implementation of the Guo-forcing scheme is from the fact that the velocity \mathbf{u}
500 that enters the expression for f^{eq} in equation (A 3) is the same as the hydrodynamic velocity
501 obtained in equation (A 9). This isn't the case for other forcing schemes.

502 The addition of a heat source term (thermal forcing term) is performed according to (Seta

503 2013) with

$$504 \quad q_i = \left(1 - \frac{1}{2\tau_g}\right) w_i \Phi \Delta t, \quad (\text{A } 10)$$

505 where $\Phi = -\alpha(T - T_p)$ is the required source term. The temperature is then obtained at each
506 lattice grid point from the thermal populations g_i as

$$507 \quad T = \sum_i g_i + \left(1 - \frac{1}{2\tau_g}\right) \Phi. \quad (\text{A } 11)$$

508 The no-slip boundary condition for the velocity at the top and bottom walls are imposed
509 using the bounce-back method (Ladd 1994). The adiabatic boundary condition for the top
510 and bottom walls are imposed using the Inamuro method for setting the normal flux at a
511 boundary for an advected scalar in a fluid (Yoshino & Inamuro 2003) by setting the flux
512 equal to 0.

513 Appendix B. Effects of varying α_0 and c

514 It is clear from the main text that an increase in the number of particles N_p strongly pushes the
515 system towards the convective configuration while increasing T_+ weakly causes the system
516 to tend towards stability. The other ways a phase change from a stable configuration to a
517 convective configuration can be triggered is by increasing the fluid-particle coupling strength
518 α_0 or the size of the particle c , both of which serve to increase the typical velocity u_0 .

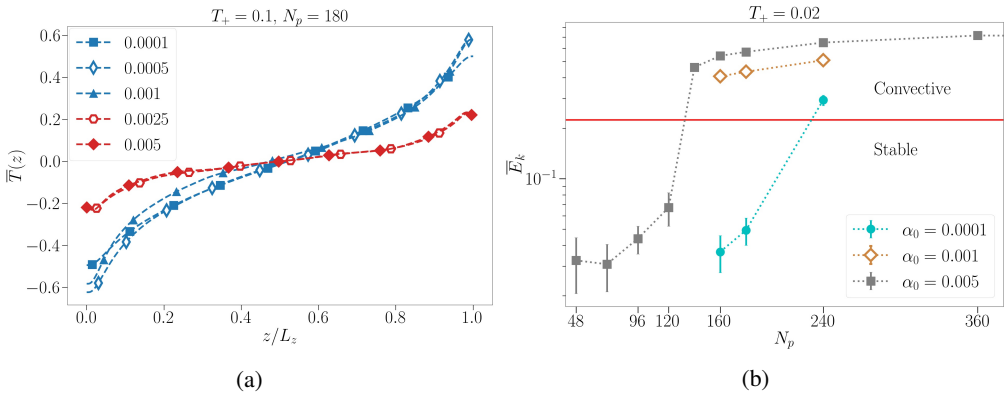


Figure 11: (a) Normalised vertical temperature profiles for $T_+ = 0.01$, $N_p = 180$ for different α . The red curves correspond to convective flows while the blue curves represent the stable flows. (b) Normalised TKE for $T_+ = 0.02$ plotted against N_p for 3 values of α_0 .

Horizontal red line represents $E_k^0 = 0.225$.

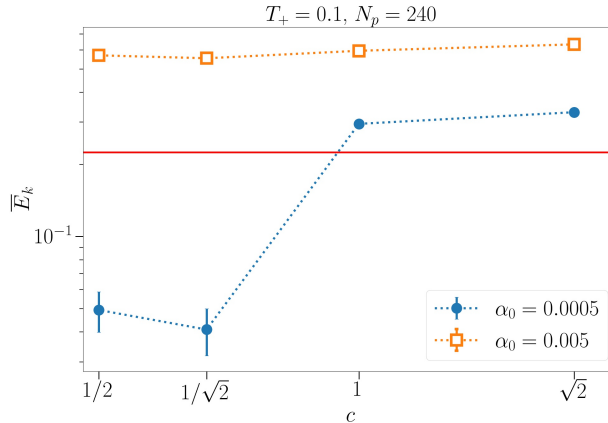


Figure 12: Normalised TKE for varying virtual particle size c for two different α_0 .

519 The former effect can be gauged in figure 11. In panel (a), we see the behavior of
 520 the temperature profile for varying α_0 . It has already been seen that the stable regime
 521 is characterised by a strongly stable temperature profile while the convective regime is
 522 characterised by a weakly stable temperature gradient. The temperature profile remains
 523 nearly identical for changing values of α_0 except when the flow changes from stable (blue
 524 curves) to convective (red curves). We also note that the time taken for the flow to relax
 525 from the initial unstable configuration (see equation (2.11)) to the eventual stationary state
 526 is larger for smaller α_0 . It indicates that for a given temperature scale T_+ and N_p , there exists
 527 a temperature difference $\overline{\Delta T}$ for which the flow is stable independent of α_0 . Panel (b) of the
 528 same figure where we plot the average normalised TKE \overline{E}_k shows the transition from stable
 529 to convective for 3 different α_0 . That the increase in TKE corresponds to the transition from
 530 stable to convective was verified from visualisations of the flow field as well as the strength
 531 of the large-scale circulation as already discussed in Section 3.2. We see that decreasing
 532 α_0 increases the N_p of the transition and still note that the empirical value of E_k^0 for the
 533 transition holds.

534 Increasing c too shows a similar effect, as clear in figure 12 where keeping the other
 535 parameters fixed, a transition to convective configuration is triggered by enlarging the size
 536 of the individual virtual particle.

537 Appendix C. Thermal Dissipation

538 We define the thermal dissipation rate as standard in the turbulence literature as

$$539 \quad \epsilon_T \equiv \kappa \langle (\partial_i T(\mathbf{x}, t))^2 \rangle_V, \quad (\text{C } 1)$$

540 and note that in the statistically stationary regime, the thermal dissipation is equal to the
 541 thermal injection. We have the heat equation given by

$$542 \quad \partial_t T + \mathbf{u} \cdot \nabla T = \kappa \nabla^2 T + \Phi. \quad (\text{C } 2)$$

543 Following (Siggia 1994) and as shown explicitly by Ching (2014, pp. 5-7) for the Rayleigh-
 544 Bénard convection, we multiply equation (C2) with T and average over the entire domain

and time to give

545

$$\begin{aligned} 546 \quad \frac{1}{2} \frac{d\langle T^2 \rangle_{V,t}}{dt} + \frac{1}{2} \langle \mathbf{u} \cdot \nabla(T^2) \rangle_{V,t} - \langle \Phi T \rangle_{V,t} \\ 547 \quad = \kappa \langle T \nabla^2 T \rangle_{V,t} = \kappa \langle \nabla \cdot (T \nabla T) \rangle_{V,t} - \kappa \langle |\nabla T|^2 \rangle_{V,t}, \quad (\text{C3}) \end{aligned}$$

548 and then use the stationary condition ($\partial_t \langle \cdot \rangle_{V,t} = 0$) and the incompressibility ($\nabla \cdot \mathbf{u} = 0$)
549 condition to give

$$550 \quad \langle \mathbf{u} \cdot \nabla(T^2) \rangle_V = \langle \nabla \cdot (\mathbf{u} T^2) \rangle_V = 0. \quad (\text{C4})$$

551 Then, equation (C3) becomes

$$552 \quad \kappa \langle |\nabla T|^2 \rangle_{V,t} = \kappa \langle \nabla \cdot (T \nabla T) \rangle_{V,t} + \langle \Phi T \rangle_{V,t}, \quad (\text{C5})$$

553 or

$$554 \quad \epsilon_T = \kappa \langle \nabla \cdot (T \nabla T) \rangle_{V,t} + \langle \Phi T \rangle_{V,t} \quad (\text{C6})$$

555 The first term of ϵ_T can further be simplified using the Gauss theorem and writing it in terms
556 of a surface integral

$$557 \quad \kappa \langle \nabla \cdot (T \nabla T) \rangle_{V,t} = \frac{\kappa}{L_z} \left[\left\langle T \partial_z T \right\rangle_{z=L_z} - \left\langle T \partial_z T \right\rangle_{z=0} \right]. \quad (\text{C7})$$

558 In this study, we set $\partial_z T = 0$ at $z = 0$ and $z = L_z$. Thus, finally we get simply

$$559 \quad \epsilon_T = \langle \Phi T \rangle_{V,t}. \quad (\text{C8})$$

REFERENCES

- 560 AHLERS, GUENTER, GROSSMANN, SIEGFRIED & LOHSE, DETLEF 2009 Heat transfer and large scale dynamics
561 in turbulent Rayleigh-Bénard convection. *Reviews of Modern Physics* **81** (2), 503.
- 562 BEC, JÉRÉMIE, HOMANN, HOLGER & RAY, SAMRIDDI SANKAR 2014 Gravity-driven enhancement of heavy
563 particle clustering in turbulent flow. *Physical Review Letters* **112** (18), 184501.
- 564 BEINTEMA, GERBEN, CORBETTA, ALESSANDRO, BIFERALE, LUCA & TOSCHI, FEDERICO 2020 Controlling
565 Rayleigh-Bénard convection via reinforcement learning. *Journal of Turbulence* **21** (9-10), 585–605.
- 566 CARBONE, MAURIZIO, BRAGG, ANDREW D & IOVIENO, MICHELE 2019 Multiscale fluid-particle thermal
567 interaction in isotropic turbulence. *Journal of Fluid Mechanics* **881**, 679–721.
- 568 CENCINI, M, BEC, J, BIFERALE, L, BOFFETTA, GUIDO, CELANI, A, LANOTTE, AS, MUSACCHIO, S & TOSCHI,
569 F 2006 Dynamics and statistics of heavy particles in turbulent flows. *Journal of Turbulence* **7**, N36.
- 570 CHING, EMILY SC 2014 *Statistics and scaling in turbulent Rayleigh-Bénard convection*. Springer.
- 571 ELPERIN, TOV, KLEEORIN, NATHAN & ROGACHEVSKII, IGOR 1996 Turbulent thermal diffusion of small inertial
572 particles. *Physical Review Letters* **76** (2), 224.
- 573 FALKOVICH, GREGORY, FOUXON, A & STEPANOV, MG 2002 Acceleration of rain initiation by cloud turbulence.
574 *Nature* **419** (6903), 151–154.
- 575 FERNANDO, HARINDRA JS, ZAJIC, DRAGAN, DI SABATINO, SILVANA, DIMITROVA, RENETA, HEDQUIST, BRENT
576 & DALLMAN, ANN 2010 Flow, turbulence, and pollutant dispersion in urban atmospheres. *Physics of*
577 *Fluids* **22** (5), 051301.
- 578 GAYEN, BISHAKHDATTA, GRIFFITHS, ROSS W & HUGHES, GRAHAM O 2014 Stability transitions and turbulence
579 in horizontal convection. *Journal of Fluid Mechanics* **751**, 698–724.
- 580 GUO, ZHAOLI, ZHENG, CHUGUANG & SHI, BAOSHANG 2002 Discrete lattice effects on the forcing term in the
581 lattice Boltzmann method. *Physical Review E* **65**, 046308.
- 582 HE, XIAOYI, CHEN, SHIYI & DOOLEN, GARY D. 1998 A novel thermal model for the lattice Boltzmann
583 method in incompressible limit. *Journal of Computational Physics* **146** (1), 282 – 300.
- 584 IRANNEJAD, ABOLFAZL, BANAEIZADEH, ARAZ & JABERI, FARHAD 2015 Large eddy simulation of turbulent
585 spray combustion. *Combustion and Flame* **162** (2), 431–450.
- 586 KIM, HOJONG, BOYSEN, DANE A, NEWHOUSE, JOCELYN M, SPATOCO, BRIAN L, CHUNG, BRICE, BURKE,

- 587 PAUL J, BRADWELL, DAVID J, JIANG, KAI, TOMASZOWSKA, ALINA A, WANG, KANGLI & OTHERS 2013
 588 Liquid metal batteries: past, present, and future. *Chemical Reviews* **113** (3), 2075–2099.
- 589 LADD, ANTHONY JC 1994 Numerical simulations of particulate suspensions via a discretized boltzmann
 590 equation. part 1. theoretical foundation. *Journal of fluid mechanics* **271**, 285–309.
- 591 LAY, THORNE, HERNLUND, JOHN & BUFFETT, BRUCE A 2008 Core-mantle boundary heat flow. *Nature*
 592 *Geoscience* **1** (1), 25–32.
- 593 LIMARE, ANGELA, VILELLA, KENNY, DI GIUSEPPE, ERIKA, FARNETANI, CG, KAMINSKI, E, SURDUCAN,
 594 EMANOIL, SURDUCAN, VASILE, NEAMTU, CAMELIA, FOUREL, LOÏC & JAUPART, CLAUDE 2015
 595 Microwave-heating laboratory experiments for planetary mantle convection. *Journal of Fluid*
 596 *Mechanics* **777**, 50–67.
- 597 LOHSE, DETLEF & XIA, KE-QING 2010 Small-scale properties of turbulent rayleigh-bénard convection.
 598 *Annual Review of Fluid Mechanics* **42**, 335–364.
- 599 MARKOWSKI, PAUL 2007 An overview of atmospheric convection. *Atmospheric Convection: Research and*
 600 *Operational Forecasting Aspects* pp. 1–6.
- 601 MARSHALL, JOHN & SCHOTT, FRIEDRICH 1999 Open-ocean convection: Observations, theory, and models.
 602 *Reviews of Geophysics* **37** (1), 1–64.
- 603 MAZIN, ILIA 1999 The effect of condensation and evaporation on turbulence in clouds. *Atmospheric Research*
 604 **51** (2), 171–174.
- 605 PARK, HYUNGWON JOHN, O'KEEFE, KEVIN & RICHTER, DAVID H 2018 Rayleigh-Bénard turbulence modified
 606 by two-way coupled inertial, nonisothermal particles. *Physical Review Fluids* **3** (3), 034307.
- 607 SALESKY, ST & ANDERSON, W 2018 Buoyancy effects on large-scale motions in convective atmospheric
 608 boundary layers: implications for modulation of near-wall processes. *Journal of Fluid Mechanics*
 609 **856**, 135–168.
- 610 SETA, TAKESHI 2013 Implicit temperature-correction-based immersed-boundary thermal lattice Boltzmann
 611 method for the simulation of natural convection. *Physical Review E* **87**, 063304.
- 612 SIGGIA, ERIC D 1994 High Rayleigh number convection. *Annual Review of Fluid Mechanics* **26** (1), 137–168.
- 613 SQUIRES, KYLE D & EATON, JOHN K 1991 Preferential concentration of particles by turbulence. *Physics of*
 614 *Fluids A: Fluid Dynamics* **3** (5), 1169–1178.
- 615 TANG, JIE & BAU, HAIM H 1994 Stabilization of the no-motion state in the Rayleigh-Bénard problem.
 616 *Proceedings of the Royal Society of London. Series A: Mathematical and Physical Sciences*
 617 **447** (1931), 587–607.
- 618 TRITTON, DJ 1975 Internally heated convection in the atmosphere of venus and in the laboratory. *Nature*
 619 **257** (5522), 110–112.
- 620 WANG, QI, LOHSE, DETLEF & SHISHKINA, OLGA 2021 Scaling in internally heated convection: a unifying
 621 theory. *Geophysical Research Letters* **48** (4), e2020GL091198.
- 622 XI, HENG-DONG, ZHANG, YI-BAO, HAO, JIAN-TAO & XIA, KE-QING 2016 Higher-order flow modes in
 623 turbulent Rayleigh-Bénard convection. *Journal of Fluid Mechanics* **805**, 31–51.
- 624 YANG, TS & SHY, SS 2005 Two-way interaction between solid particles and homogeneous air turbulence:
 625 particle settling rate and turbulence modification measurements. *Journal of Fluid Mechanics* **526**,
 626 171–216.
- 627 YOSHINO, MASATO & INAMURO, TAKAHI 2003 Lattice boltzmann simulations for flow and heat/mass transfer
 628 problems in a three-dimensional porous structure. *International journal for numerical methods in*
 629 *fluids* **43** (2), 183–198.
- 630 ZAMANSKY, RÉMI, COLETTI, FILIPPO, MASSOT, MARC & MANI, ALI 2014 Radiation induces turbulence in
 631 particle-laden fluids. *Physics of Fluids* **26** (7), 071701.
- 632 ZAMANSKY, RÉMI, COLETTI, FILIPPO, MASSOT, MARC & MANI, ALI 2016 Turbulent thermal convection
 633 driven by heated inertial particles. *Journal of Fluid Mechanics* **809**, 390–437.